



Heat-affected zone property diagrams for a grade 100 microalloyed steel

Kioumars Poorhaydari¹ · Douglas G. Ivey¹

Received: 11 October 2017 / Accepted: 24 January 2018 / Published online: 7 February 2018
© International Institute of Welding 2018

Abstract

The microhardness variations and microstructural alterations in the heat-affected zone (HAZ) of a grade 100 steel, microalloyed with titanium, niobium, and vanadium were examined for a range of heat inputs from 0.3 to 2.5 kJ/mm. The results of the precipitate dissolution analysis and weld thermal analysis were used to establish HAZ property diagrams and qualitatively explain grain size and microhardness profiles across the HAZ for different heat input values. The relative width of the coarse-grained HAZ (CGHAZ) increased and the grain coarsening temperature decreased with decreasing heat input, although the amount of grain growth decreased with decreasing heat input. Detailed microstructural examination using a transmission electron microscope (TEM) coupled with nanohardness measurements showed that the CGHAZ was not 100% martensite even at a low heat input of 0.5 kJ/mm, while the micro- and macrohardness values suggested a “fully martensitic” structure. Microhardness testing also revealed that the maximum HAZ hardness was in the CGHAZ at some distance from the fusion line, as opposed to being adjacent to the fusion line.

Keywords Microalloyed steels · Welding · Heat-affected zone · Hardness · Electron microscopy · Martensite

1 Introduction

Low-carbon microalloyed steels are a group of high-strength low-alloy (HSLA) steels produced in the as-rolled condition. Thermomechanical controlled processing (TMCP) and the addition of a small amount of microalloying elements, such as titanium, niobium, and vanadium, lead to grain refinement and precipitation hardening that result in high strength values without sacrificing ductility or weldability [1, 2].

The weld thermal cycle causes phase transformations, grain size changes, and precipitate alterations that affect the mechanical properties of the heat-affected zone (HAZ). Excessive hardening and softening in the WM/HAZ are both undesirable. Hardening in high-strength microalloyed or low-alloy steels may make the steel

potentially susceptible to cold cracking after welding or environment-assisted cracking in service. Softening can also be deleterious, due to the possible occurrence of “concentrated strain” that can lead to ductile fracture [3]. As such, hardness variation in the HAZ should be monitored so that no drastic hardening or softening occurs. One of the most practical welding parameters that affect the HAZ properties is weld heat input. It is, therefore, necessary to understand the microstructural and microhardness changes within different sub-regions of the HAZ for different heat inputs in new grades of high-strength microalloyed steel. This is the main reason for studying grade 100 microalloyed steel as it is a relatively new material. In addition, other questions arose during the investigation, particularly regarding martensite formation and character, which are also addressed.

Hence, the objectives of this article are (1) to establish HAZ property diagrams that present and combine microhardness profiles, grain size profiles, HAZ sub-region widths, peak temperatures at the sub-region boundaries, and precipitate dissolution amounts across the HAZ and (2) to evaluate martensite formation and character (type, size, and hardness) in the coarse-grained HAZ (CGHAZ) of this particular grade of low-carbon microalloyed steel when welded with low heat input values (i.e., 0.5 kJ/mm or lower). This article combines the

Recommended for publication by Commission IX - Behaviour of Metals Subjected to Welding

✉ Kioumars Poorhaydari
kioumars@ualberta.ca

¹ Department of Chemical and Materials Engineering, University of Alberta, Edmonton, AB T6G 1H9, Canada

results of several earlier studies (presented elsewhere) in order to establish the HAZ property diagrams. As such, the main results of the various studies (namely thermal analysis, grain size variations, phase transformations, and precipitate alterations) are reviewed briefly, while more emphasis is placed on the results of microhardness and microstructural examinations, particularly of the martensitic phase.

2 Experimental procedure

Tables 1 and 2 show the chemical composition and the basic mechanical properties of the 8-mm wall thickness, grade 100 microalloyed steel plate used in this study. Weld samples were produced by autogenous gas tungsten arc welding. Nominal heat inputs of 0.3 to 2.5 kJ/mm were applied by selecting an arc current of 150 A, an arc voltage of 12.5 V, and travel speeds of 0.7 to 6.0 mm/s. For some examinations (such as microstructural evaluation), three heat input values of 0.5, 1.5, and 2.5 kJ/mm were chosen, while more heat input values were selected for some other examinations (such as microhardness traverses across the HAZ). A full description of the welding process, temperature acquisition, and thermal analysis is given elsewhere [4].

Standard metallographic samples were prepared from both transverse and longitudinal sections (with respect to the welding direction) and etched with 2% Nital. Two types of TEM samples were prepared from four distinct regions, namely the base metal (BM), inter-critical HAZ (ICHAZ), fine-grained HAZ (FGHAZ), and CGHAZ. The types of samples were conventional carbon extraction replicas [5] and site-specific thin-foil samples prepared by a focused ion beam (FIB) technique. TEM samples were examined in a JEOL 2010 TEM operated at 200 kV and equipped with an ultra-thin-window energy-dispersive X-ray (EDX) system.

Vickers hardness tests, with loads of 5 kg and 500 g, were used to obtain the average macrohardness number in the middle of each sub-region and the microhardness profile across the HAZ, respectively. A Mitutoyo hardness tester was used for macro- as well as microhardness measurements. Nanohardness measurements were carried out at selected sub-regions with a Hysitron® nanomechanical probe with a load of 500 μ N and hardness numbers in GPa were calculated for each point [6].

Table 1 Chemical composition of grade 100 microalloyed steel (wt%)

C	Mn	Ti	Nb	V	Mo	N	Others	P_{cm} ^a
0.08	1.80	0.06	0.09	0.05	0.30	0.01	<1.2	0.24

^aIto-Bessyo critical metal parameter

3 Results

3.1 Thermal analysis

Four thermal cycles, at different distances from the fusion line, were obtained for three heat input values of 0.5, 1.5, and 2.5 kJ/mm, using thermocouples embedded in the weld plates. Table 3 presents the average values of thermal parameters extracted from the curves. One of these parameters is the austenite transformation temperature upon cooling in the CGHAZ that appeared as a small bump on the thermal cycle curve. The bump forms due to the release of the heat of transformation [7].

3.2 HAZ sub-region width

Different HAZ sub-regions were identified on the etched metallographic samples, as shown in Fig. 1. The sub-region widths were measured, and the average values of the measurements for the entire HAZ and the CGHAZ sub-regions for five heat input values between 0.5 and 2.5 kJ/mm are presented in Table 4. The relative width of the CGHAZ decreased with increasing heat input, which is discussed in Sect. 4.3.

3.3 Macro-, micro-, and nanohardness results

Table 5 presents the results of Vickers macrohardness testing, using a load of 5 kg, in the middle of each sub-region for three values of heat input [8]. Microhardness measurements, using a load of 500 g, were taken along radial traverses on the transverse sections through the welds. Figure 2 shows the microhardness profiles for five values of heat input, namely 0.5, 0.7, 1.0, 1.5, and 2.5 kJ/mm. Note that the sub-region boundaries are not shown accurately, as they would be somewhat different for different heat input values. For a heat input of 0.5 kJ/mm, the HAZ was too small to obtain a hardness traverse with adequate spatial resolution. As such, Vickers microhardness mapping was performed on the longitudinal section and the results are plotted in Fig. 3. The hardness mapping increased the reliability/accuracy of the measurements and the resolution of the hardness profile.

Figure 3 shows that for a heat input of 0.5 kJ/mm, there is considerable hardening from the BM (~285 HV0.5) to the CGHAZ (with a maximum of ~360 HV0.5). Initially, there is a moderate increase in the hardness across the FGHAZ reaching ~310 HV0.5, while at the boundary between the FGHAZ and CGHAZ, there is a very steep increase to ~360 HV0.5. The hardness slightly decreases across the CGHAZ towards the fusion line (~340 HV0.5). For a heat input of 0.7 kJ/mm, there is initially some softening from ~285 to ~270 HV and then some hardening to ~300 HV0.5 in the FGHAZ (Fig. 2). This heat input appears to represent the transition between hardening and softening in the

Table 2 Mechanical properties of grade 100 microalloyed steel

Modulus of elasticity (E), GPa (10^3 ksi)	Yield strength (0.2% offset), MPa (ksi)	Tensile strength, MPa (ksi)	Elongation (%)	Hardness, HV5
214.6 (31.1)	788 (114)	921 (134)	17	286

Tensile properties were obtained in the longitudinal direction from the plate and are the average of three measurements

FGHAZ. For the higher heat inputs, however, softening is predominant across the FGHAZ, i.e., the hardness drops from ~ 285 to ~ 250 HV0.5.

Microhardness profiles for lower heat inputs than 0.5 kJ/mm (i.e., 0.3 and 0.4 kJ/mm) were also obtained in the CGHAZ to see the relationship between maximum HAZ hardness and heat input. Table 6 summarizes the results. The 0.3 kJ/mm sample showed markedly higher hardness values, with an average of approximately 364 HV0.5 and a maximum hardness of 375 HV0.5. Figure 4 shows that there is a relatively linear relationship between CGHAZ maximum hardness and heat input. An important observation is that the microhardness number does not reach a plateau over the range of heat inputs examined and the number can reach as high as 375 HV0.5. This finding is discussed in Sect. 4.4.

As the microstructural constituents in the HAZ are often only a few microns, or even sub-micron, in size, nanohardness mapping was employed to obtain the hardness contours in selected sub-regions. Figure 5 shows hardness contours for the CGHAZ of the 0.5 kJ/mm weld sample and the BM, taken over an area of approximately $3 \mu\text{m} \times 4 \mu\text{m}$. In addition to showing higher hardness levels for the CGHAZ than the base metal, the contours reveal that both regions are made up of a mixture of microstructural constituents with different hardness values (as discussed in Sect. 4.2.3).

3.4 Grain-size profiles

The grain sizes (or more accurately the mean linear intercepts) were measured across the HAZ for two heat input values of 0.5 and 2.5 kJ/mm using optical microscopy (OM). The details and the results of grain size measurements are presented elsewhere [9], and the results are incorporated in the HAZ

property diagrams that are presented and discussed in Sect. 4.2. The main findings are briefly reviewed here.

Although the average sizes were somewhat larger for the higher heat input, the grain size variations exhibited similar trends. Both samples exhibited a plateau in the FGHAZ and an abrupt continuous grain size increase in the CGHAZ towards the fusion line. The plateau in the FGHAZ was due to the low mobility of the prior austenite grain boundaries (associated with relatively low peak temperatures), as well as restriction of prior austenite grain growth by the pinning action of undissolved precipitates and the solute drag effect of alloying elements from the dissolved precipitates. In the CGHAZ, austenite grain growth occurs with little restriction and the prior austenite grain size (PAGS) increases with increasing peak temperature (i.e., decreasing distance from the fusion line).

3.5 Microstructures

Carbon extraction replicas, imaged at a relatively low magnification in the TEM, were utilized for general examination of the microstructures in these regions, since many of the grains in the BM and HAZ were too small to be resolved by OM. The BM is made up primarily of packets of oriented bainitic ferrite along with dark-etching regions that are likely carbon-rich martensite/retained-austenite (M/A) constituents. The BM microstructure is examined in detail elsewhere [2]. The HAZ microstructures were examined for three heat input values (0.5, 1.5, and 2.5 kJ/mm) and at different sub-regions (i.e., ICHAZ, FGHAZ, and CGHAZ). The major findings are as follows.

The ICHAZ (all samples) exhibited a mixture of untransformed bainitic ferrite and retransformed polygonal ferrite. Basically, the microstructure is something between that of the BM and the FGHAZ, as transformation to austenite during

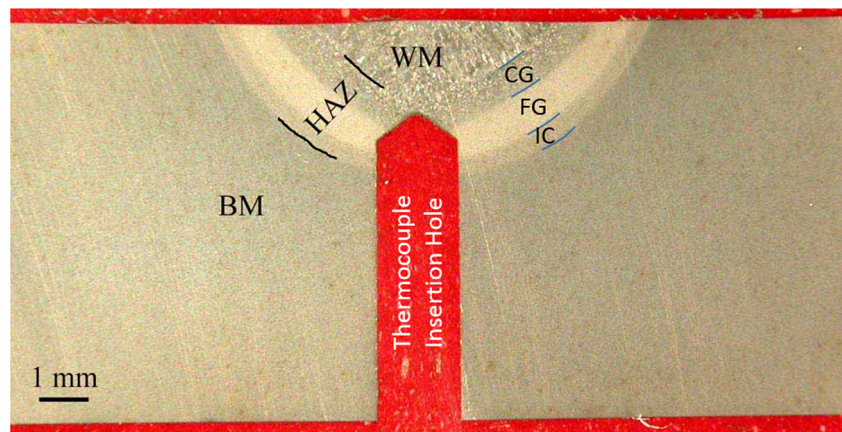
Table 3 Weld thermal parameters

Nominal heat input (kJ/mm)	Heating rate ($^{\circ}\text{C/s}$)	Cooling time (Δt_{8-5}) (s) ^a	Mean cooling rate ($^{\circ}\text{C/s}$) ^b	Cooling rate at 550 $^{\circ}\text{C}$ ($^{\circ}\text{C/s}$)	CGHAZ transformation temperature ($^{\circ}\text{C}$)
0.5	1537 ± 857	1.8 ± 0.1	171.0 ± 6.2	111.7 ± 7.2	400–430
1.5	248 ± 151	17.2 ± 1.5	16.8 ± 1.2	10.9 ± 1.2	470–480
2.5	70 ± 20	37.7 ± 10.1	8.0 ± 2.9	6.1 ± 2.2	500–510

^a Δt_{8-5} is the cooling time from 800 to 500 $^{\circ}\text{C}$

^b The mean cooling rate was obtained by dividing the temperature range of 300 $^{\circ}\text{C}$ by the cooling time

Fig. 1 HAZ sub-region boundaries on a transverse cross section (0.5 kJ/mm)



the heating portion of the weld thermal cycle is not completed in this sub-zone.

Figure 6 compares the FGHAZ microstructures for heat input values of 0.5 and 1.5 kJ/mm. In the FGHAZ-0.5 kJ/mm sample, several types of ferrite were identified. The region labeled 1 contains polygonal ferrite, which is distinct from the bainitic ferrite (marked as region 2) with large aspect ratios and appearing in packets. The rest of the grains have structures between polygonal ferrite and lath-like bainitic ferrite; they are likely acicular ferrite. The FGHAZ for heat inputs of 1.5 and 2.5 kJ/mm consists mainly of polygonal ferrite. Transformation to austenite during the heating portion of the weld thermal cycle is completed in this sub-zone. The higher cooling rate (10–20 times higher; Table 3) associated with the heat input of 0.5 kJ/mm increased the chance of formation of acicular and bainitic structures, even though the PAGS was small and grain growth was suppressed in this region.

Figure 7 shows examples of CGHAZ microstructure for the heat input of 0.5 kJ/mm. Figure 7a exhibits a typical prior austenite grain, containing packets of lath martensite (LM). Four packets were identified in this prior austenite grain (one of which is indicated as region “1”), consistent with orientation relationship (OR) studies [10]. There are four variants of the $\{111\}\gamma$ planes in the Kurdjumov-Sachs OR. There are theoretically six lath orientation variants, which should result in the formation of six lath blocks within each packet,

while each block contains a few laths with the same orientation. Identification of the blocks and laths was beyond the scope of work in this study.

Although a lath martensitic microstructure is a major morphology in the CGHAZ-0.5 kJ/mm sample, other morphologies were also found. Another major microstructure present in many regions is wide plates of ferrite with intermediate-size particles inside. One of these regions is indicated in Fig. 7a as region “2.” This microstructure, referred to as coarse autotempered (lath) martensite by some researchers [11, 12], is also indicated by arrows in Fig. 7b, c. It has a width of 2–4 μm . The cementite particles, which are a few hundred nanometers in length (Fig. 7d), exhibited certain angles, suggestive of an OR with the matrix which is a characteristic of autotempered martensite. Another morphological feature is the formation of triangles of lath martensite; one such feature is marked in Fig. 7c. The triangular formation is due to variants of the orientation relationship between the laths and the prior austenite. A very minor structure is grain-boundary ferrite (GF), as indicated by an arrow in Fig. 7a.

Coarse martensite forms first from austenite (at relatively high temperatures) and as a result is autotempered, while fine lath martensite forms at lower temperatures and is relatively heavily dislocated and untempered [11]. Another explanation is provided by Speich and Warlimont [13], who found massive ferrite along with lath martensite in quenched low-carbon irons. Cementite precipitation in massive ferrite takes place

Table 4 HAZ width measurements

Nominal heat input (kJ/mm)	HAZ width (mm)	CGHAZ width (mm)	CGHAZ width fraction
0.5	1.90	0.60	0.32
0.7	2.45	0.75	0.31
1.0	3.00	0.90	0.30
1.5	4.70	1.20	0.26
2.5	7.30 ^a	1.70	0.23

^a Estimated based on extension of the HAZ boundary curves; the HAZ of the 2.5 kJ/mm sample intersected with the bottom surface of the plate

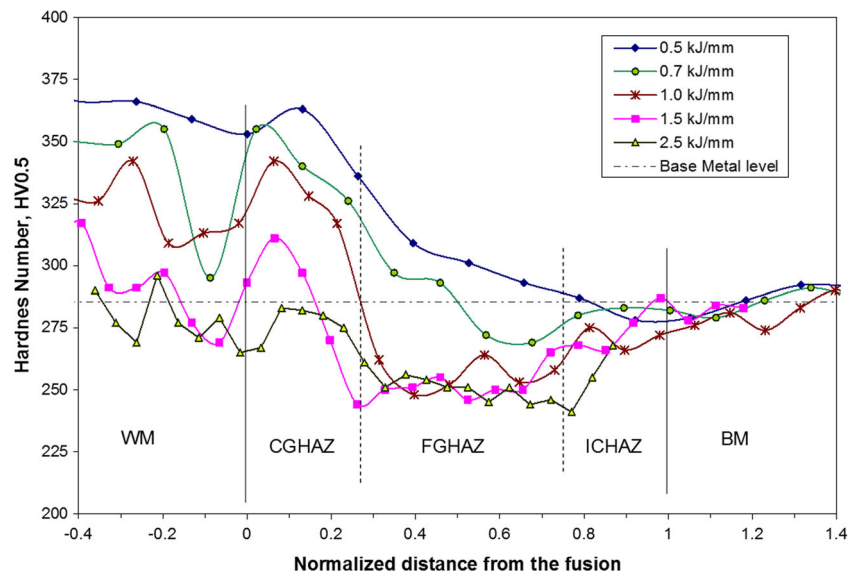
Table 5 Average macrohardness numbers (HV5) at the middle of each sub-region

Heat input (kJ/mm)	ICHAZ	FGHAZ	CGHAZ
0.5	291 ± 1	304 ± 3	355 ± 3
1.5	281 ± 1	252 ± 2	291 ± 3
2.5	N.A. ^a	249 ± 2	270 ± 5

Source: [8]

^a Due to the large size of the HAZ (2.5 kJ/mm), the ICHAZ was not available on the longitudinal section

Fig. 2 Microhardness profiles across the HAZ for a range of heat inputs



after aging at room temperature for several days. Massive ferrite forms at higher temperatures through a massive transformation mechanism. These findings indicate that the microstructure, although mainly martensitic (and classically referred to as “fully martensitic,” when examined by OM only), is not 100% lath martensite. As the carbon level decreases in steel, formation of martensite becomes more difficult [13].

The CGHAZ-1.5 kJ/mm microstructure exhibited packets of dense bainitic ferrite laths within the large prior austenite grains (see region 1 in Fig. 8a). The main constituents in this sample are granular bainite, comprised of massive ferrite (MF) and granules of M/A constituents or bainitic laths, lower bainite (LB) and GF (Fig. 8b, c). Cementite particles were identified within LB by a combination of energy-dispersive X-ray (EDX) spectroscopy and selected area diffraction (SAD) patterns (not presented here). The formation of cementite (Fe_3C)

can be a result of a moderate cooling rate during the weld thermal cycle (1.5 kJ/mm), which is too fast for the precipitation of more stable microalloyed carbides. The availability of Fe atoms for the formation of cementite compensates for its higher solubility compared with microalloy carbides.

Figure 9 shows selected microstructural features in the CGHAZ-2.5 kJ/mm sample. The structure mainly consists of lath-like constituents, particularly granular bainite (Fig. 9a) with some acicular ferrite (Fig. 9b). The acicular ferrite plates, likely to have nucleated on nitrides or inclusions, appear in a triangular arrangement.

Figure 10 compares the bainite lath width in the CGHAZ-2.5 kJ/mm sample (~1–2 μm) with the martensite lath width in the CGHAZ-0.5 kJ/mm sample (~200–500 nm). The smaller lath size of martensite is a significant strengthening factor.

Fig. 3 Microhardness mapping for 0.5 kJ/mm weld sample

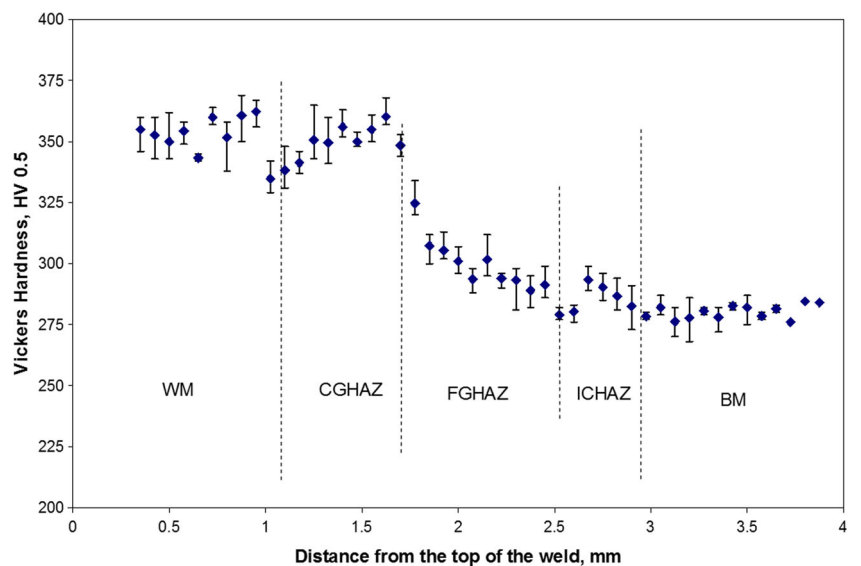


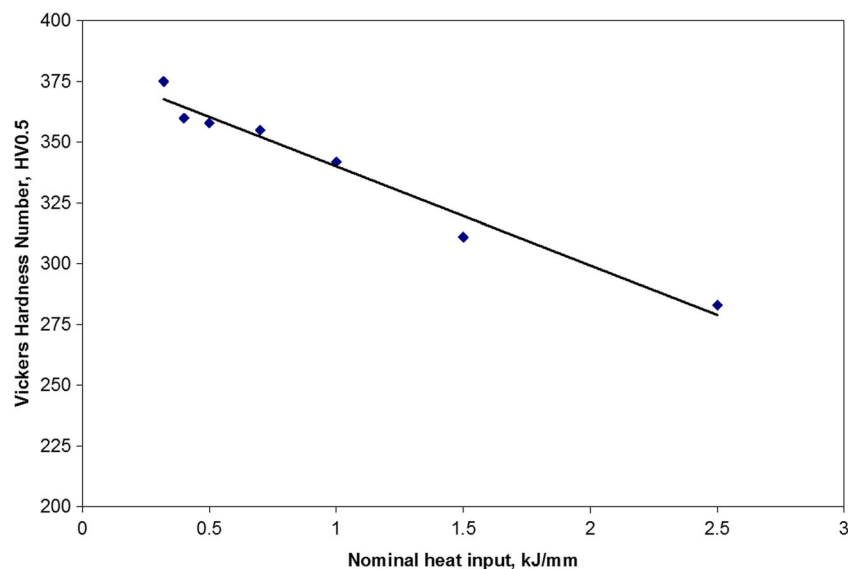
Table 6 Microhardness variation in CGHAZ for low values of heat input

Heat input (kJ/mm)	HV0.5	
	Max hardness	Average hardness
0.3	375	364 ± 7
0.4	360	350 ± 8
0.5	358	350 ± 7

3.6 Precipitates

Precipitates were examined for each sub-region and for three heat input values of 0.5, 1.5, and 2.5 kJ/mm using carbon extraction replicas, and the results were compared with theoretical calculations for precipitate dissolution. The results of these examinations were presented elsewhere [14], and a brief summary is presented here. Both theoretical calculations and experimental observations showed that particle coarsening was very limited during the fast thermal cycle of the welding, for the sizes and compositions of the precipitates present in the BM of the grade 100 steel. Precipitate dissolution was the most significant change in the HAZ of the grade 100 steel. The dissolution of Nb-rich carbonitrides started in the FGHAZ close to the boundary with the CGHAZ; the exact location depended on the heat input. Most intermediate-size Ti-Nb precipitates (50–300 nm) did not dissolve in the FGHAZ. The intermediate-size Nb-rich precipitates, however, dissolved to a large extent in the CGHAZ, especially for the higher heat inputs of 1.5 and 2.5 kJ/mm. Large Ti nitrides (2–8 μm) and intermediate-size Ti-rich carbonitrides did not change significantly in the HAZ, even in the CGHAZ. A maximum dissolution of $\sim 15\%$ was calculated for TiN close to the fusion line for a heat input of 2.5 kJ/mm.

Fig. 4 Maximum microhardness in the CGHAZ as a function of heat input



Reprecipitation was generally suppressed in the CGHAZ-0.5 kJ/mm sample. There was some reprecipitation in the CGHAZ of higher heat-input samples (in the form of fine precipitates) within the matrix, on the grain/lath boundaries and on the remaining intermediate-size precipitates.

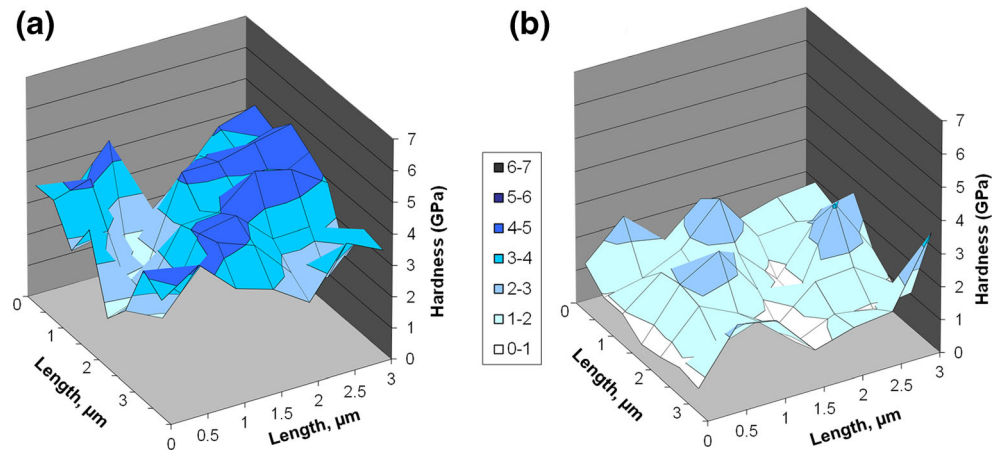
4 Discussion

4.1 Effect of weld thermal parameters

The two weld thermal parameters that affect microstructural variations across the HAZ and among the heat inputs are the peak temperature (T_p) and cooling rate (or cooling time). The time for cooling from 800 to 500 $^{\circ}\text{C}$, Δt_{8-5} , is essentially the same for all sub-regions (with the exception of the ICHAZ where the cooling rate is slightly lower for $T_p < 840$ $^{\circ}\text{C}$) and depends only on the heat input and plate thickness/geometry [15]. The difference in microstructural changes across the HAZ for different sub-zones is mainly due to the difference in T_p , which results in higher hardenability for the CGHAZ relative to the FGHAZ. The high T_p in the CGHAZ (~ 1200 – 1500 $^{\circ}\text{C}$) causes an abrupt increase in the PAGS, as well as enrichment of the austenite in microalloying elements and carbon due to dissolution of the precipitates. Both of these effects increase the hardenability, i.e., the tendency to form lower temperature transformation products such as bainite and martensite. This explains the formation of lath-like structures of martensite and bainite in the CGHAZ of grade 100 steel as opposed to polygonal ferrite (and some bainitic ferrite in the case of a low heat input of 0.5 kJ/mm) in the FGHAZ.

Decreasing the heat input results in an increase in cooling rate. A cooling rate of ~ 100 – 200 $^{\circ}\text{C/s}$ (with a mean cooling rate of 171 $^{\circ}\text{C/s}$; Table 3) resulted in a ferritic-bainitic structure in the

Fig. 5 Nanohardness contours. **a** CGHAZ-0.5 kJ/mm. **b** BM

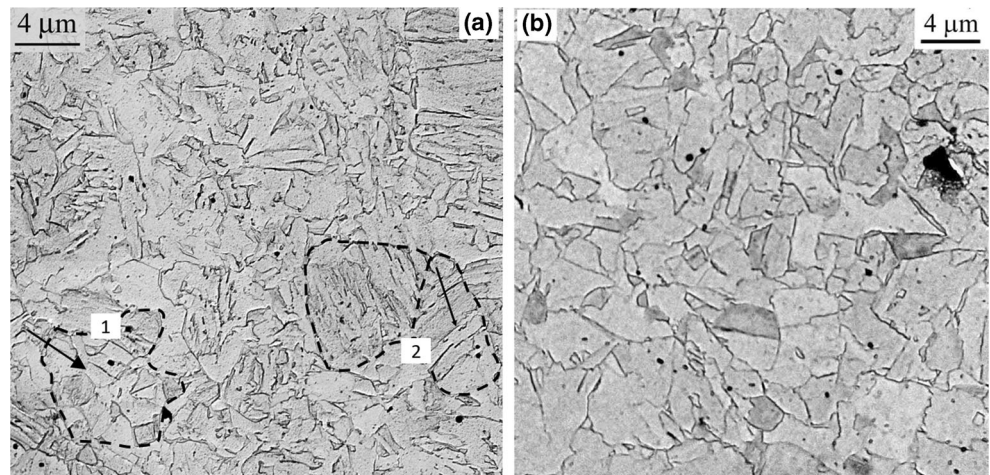


FGHAZ and a martensitic structure in the CGHAZ for a heat input of 0.5 kJ/mm. This was accompanied by a transformation temperature of $\sim 400\text{--}430\text{ }^{\circ}\text{C}$ (Table 3) in the CGHAZ, which is consistent with the formation of martensite in low-carbon HSLA steels ($M_S < 450\text{ }^{\circ}\text{C}$) as reported by Shome et al. [16] through dilatation studies. Decreasing the cooling rate to $\sim 10\text{--}20\text{ }^{\circ}\text{C/s}$ in weld samples with a heat input of 1.5 and 2.5 kJ/mm resulted in the formation of mainly polygonal ferrite in the FGHAZ and mainly bainitic ferrite in the CGHAZ (with various amounts of lower bainite, upper bainite, granular bainite, and acicular ferrite). This was accompanied by transformation temperatures of $470\text{--}480\text{ }^{\circ}\text{C}$ for a heat input of 1.5 kJ/mm and $500\text{--}510\text{ }^{\circ}\text{C}$ for a heat input of 2.5 kJ/mm in the CGHAZ. These observations are also consistent with the formation of bainitic structures in low-carbon HSLA steels.

4.2 HAZ property diagrams and microstructure-microhardness relationships

Hardness measurements across the HAZ (Fig. 2) showed variations in each sub-zone for several values of heat input (0.5, 0.7, 1.0, 1.5 and 2.5 kJ/mm). This behavior is discussed for each sub-zone and explained in terms of microstructural changes.

Fig. 6 General microstructures of the FGHAZ (TEM bright field (BF) images from replicas). **a** 0.5 kJ/mm. **b** 1.5 kJ/mm



The microstructures for a heat input of 0.5 kJ/mm showed markedly different variations than the microstructures for heat inputs of 1.5 and 2.5 kJ/mm. For this reason, the microstructure-property correlation will be explained in more detail for the two extreme heat inputs (i.e., 0.5 and 2.5 kJ/mm). Figures 11 and 12 show HAZ property diagrams for these two weld samples. The diagrams combine HAZ sub-region widths, peak temperatures at the sub-region boundaries, microhardness profiles, grain size profiles, and precipitate dissolution amounts across the HAZ.

Note that the intent of this investigation was to determine the response of the grade 100 steel (in terms of microhardness and microstructure) to a range of weld heat input values and to map out the HAZ for two selected heat input values. Since favorable properties (such as hardness and microstructure) depend on the actual engineering application and the governing specifications, a suitable heat input can be chosen from data obtained based on the actual application and corresponding criteria.

4.2.1 ICHAZ

The ICHAZ (for several heat inputs) essentially showed hardness levels between that of the BM and the FGHAZ, as

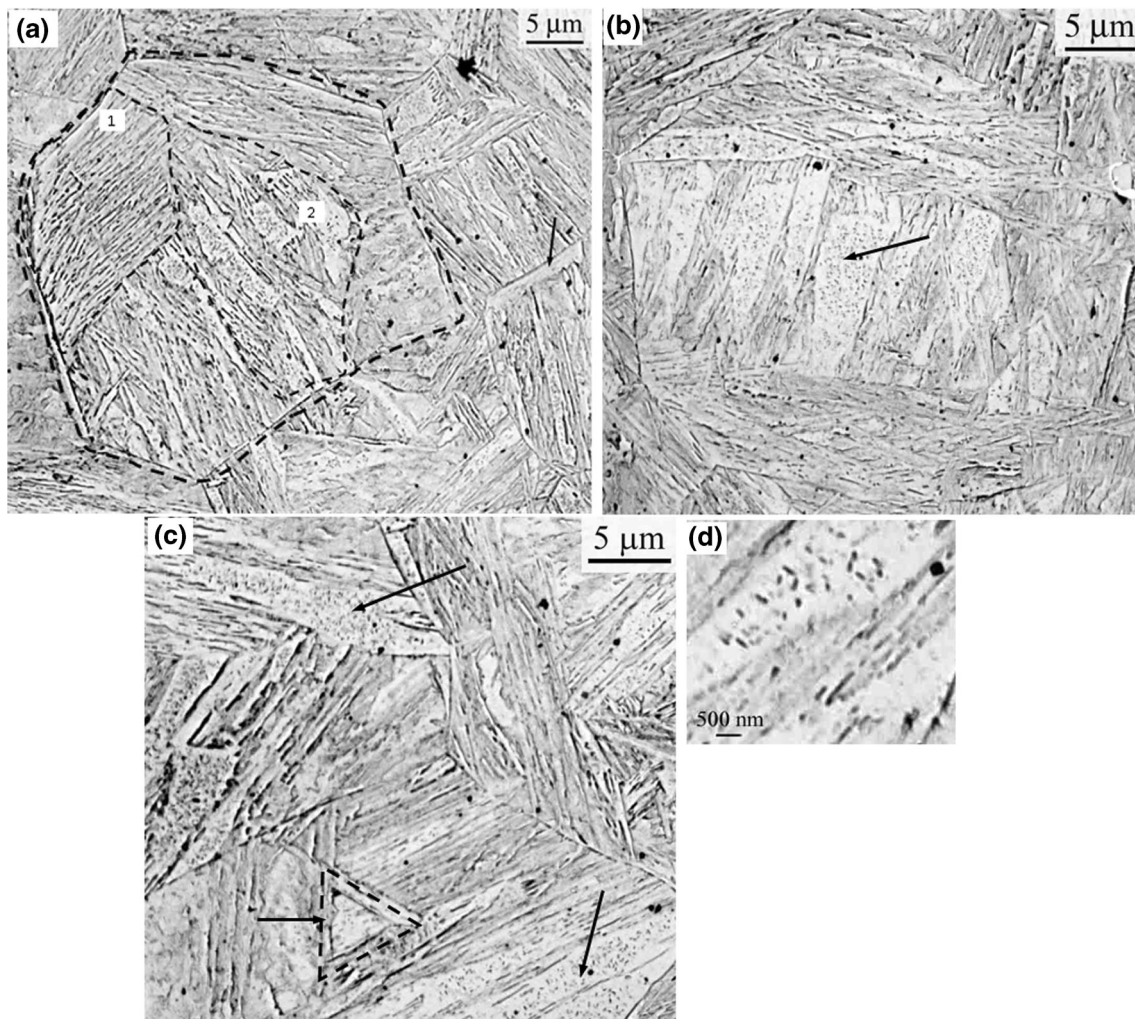


Fig. 7 **a** A typical prior austenite grain comprising four packets of martensite. **b, c.** Two examples of coarse autotempered martensite along with fine lath martensite. **d** Cementite particles within autotempered martensite matrix

expected for this sub-zone. Longitudinal mapping provided a very detailed and reliable account of hardness variation for the 0.5 kJ/mm weld sample. For this reason, the variations in the

average hardness will be assumed to be a true representation of property changes across the HAZ for this sample. The average hardness increased linearly from ~ 278 to 293 HV0.5

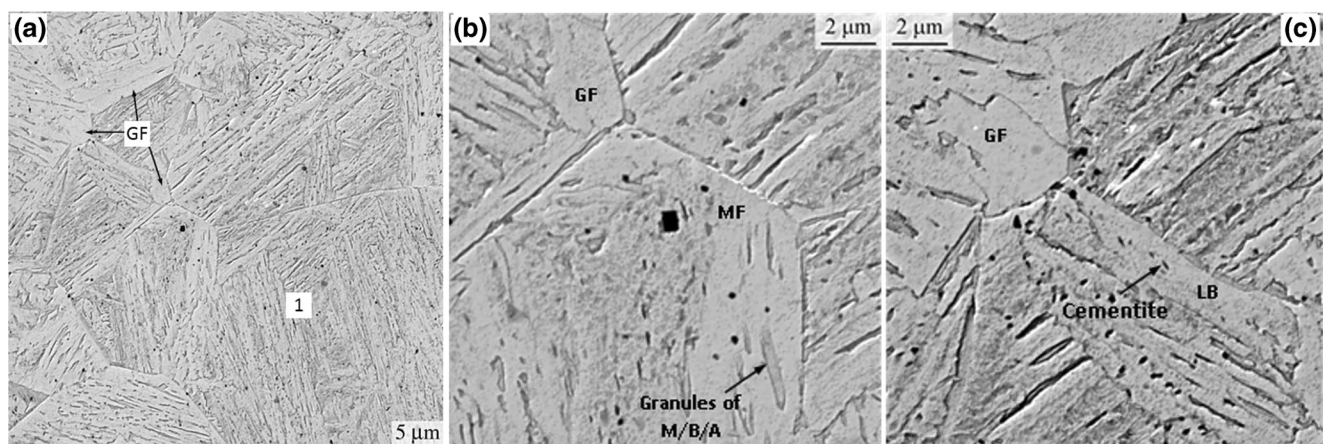
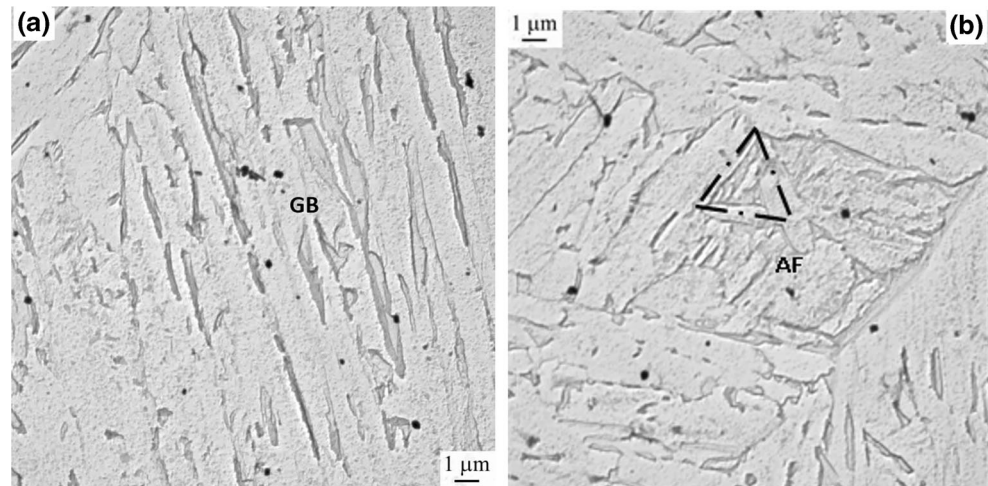


Fig. 8 **a** General structure, consisting of bainite and grain-boundary ferrite. **b** A magnified area in **a**, exhibiting granular bainite. **c** Another area in **a** exhibiting lower bainite

Fig. 9 Examples of CGHAZ microstructure for a heat input of 2.5 kJ/mm (TEM BF images from replicas) **a** granular bainite. **b** acicular ferrite



from the side adjacent to the BM towards the FGHAZ (i.e., hardening; Fig. 11). This can be attributed to the linear increase in the fraction of retransformed grains in ICHAZ. The retransformed grains will have a characteristically higher hardness than the untransformed grains due to the increase in the level of solutes (dissolution of Mo, V and Fe carbides upon austenitization) and the relatively high cooling rate ($\sim 100\text{--}200\text{ }^{\circ}\text{C/s}$ as compared with the accelerated cooling rate of $15\text{--}20\text{ }^{\circ}\text{C/s}$ during TMCP of grade 100 steel). These two factors result in finer ferrite grain sizes and slightly higher solute solution and dislocation strengthening. There is likely to be some bainitic transformation in this zone, but the likelihood of martensite formation is slim, as the combination of PAGS, cooling rate, and solute levels does not favor martensite formation.

The hardness profile for a heat input of 2.5 kJ/mm showed softening from $\sim 285\text{ HV}0.5$ at the BM boundary to $\sim 250\text{ HV}0.5$ at the FGHAZ boundary. This was a result of the lower cooling rate associated with this heat input that, as explained for the grain size in the FGHAZ, resulted in larger retransformed polygonal ferrite grains.

4.2.2 FGHAZ

In the FGHAZ, three types of behavior were observed: hardening for a heat input of 0.5 kJ/mm, a mix of softening and hardening for a heat input of 0.7 kJ/mm, and softening for heat input values of 1.0 kJ/mm and higher.

In the 0.5 kJ/mm weld sample, the average hardness increased almost linearly from ~ 291 to $307\text{ HV}0.5$ towards the CGHAZ (Fig. 11). This alteration was due to increased dissolution of V, Mo, and Fe carbides that enriched the austenite in solute levels, in particular C. As the amount of C increases towards the CGHAZ, the hardenability increases. The relatively high cooling rate in this sample makes the transformation sensitive to the C level. The combined effect of increased hardenability and high cooling rate promotes the formation of bainite. Bainitic ferrite has a higher hardness than polygonal ferrite (the dominant microstructure in the FGHAZ) due to higher solute levels in solution, higher density of transformation dislocations, and smaller grain sizes. The amount of bainitic ferrite is almost linearly proportional to the peak temperature ($\sim 800\text{ }^{\circ}\text{C} < T_p < 1190\text{ }^{\circ}\text{C}$), which increases towards

Fig. 10 CGHAZ laths (TEM BF images from FIB samples). **a** 2.5 kJ/mm. **b** 0.5 kJ/mm

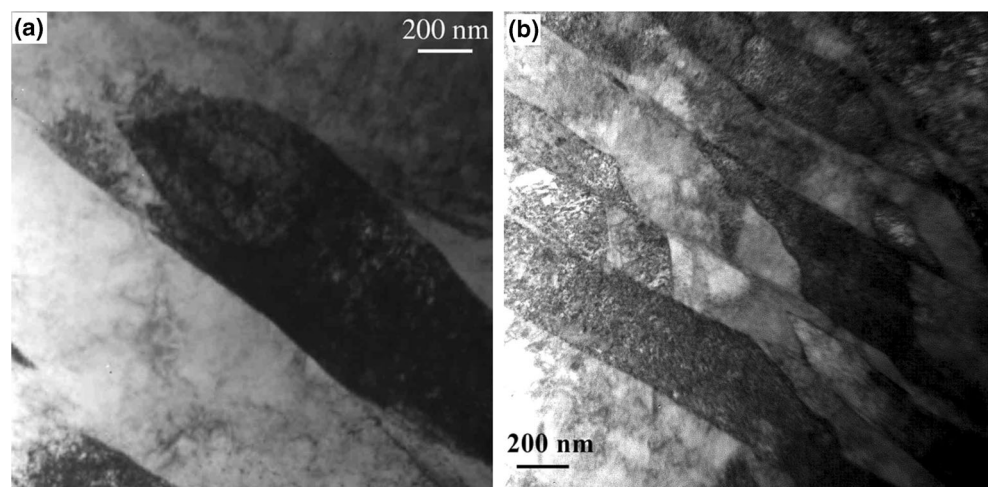
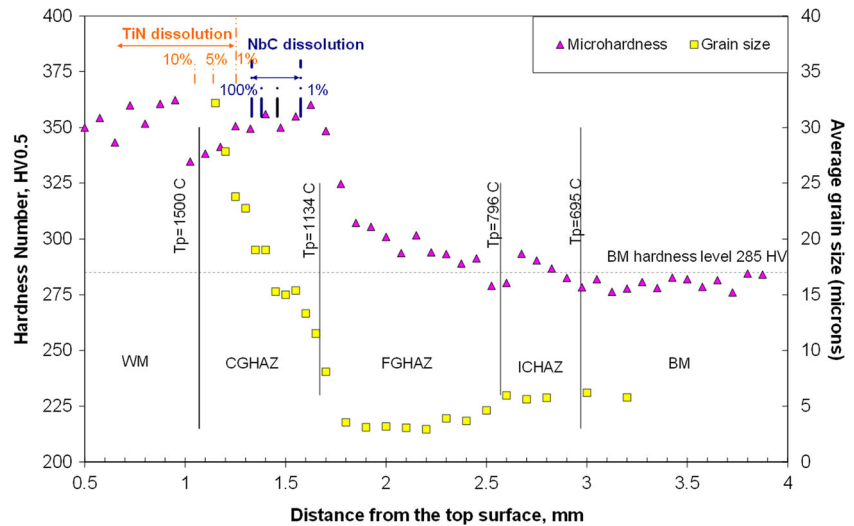


Fig. 11 HAZ property diagram for a heat input of 0.5 kJ/mm; the vertical marks in the top-left corner represent the calculated locations corresponding to a certain precipitate dissolution fraction for NbC (i.e., 1, 10, 50, and 100%) and TiN (i.e., 1, 5, and 10%)



the CGHAZ. The formation of martensite in this zone is unlikely, as the combination of PAGES and cooling rate does not favor martensite formation.

The hardness variation in the 0.7 kJ/mm weld sample showed an initial softening to a hardness of ~ 270 HV0.5 from the boundary with the ICHAZ to the mid-FGHAZ and a hardening to ~ 300 HV0.5 from the mid-FGHAZ towards the CGHAZ (Fig. 2). This suggests that the FGHAZ in this sample is actually composed of two sub-zones, an inner FGHAZ and an outer FGHAZ. This sample was not selected for thermal/microstructural examination. Nevertheless, it can be speculated that softening is due to the combination of a not-so-high cooling rate (lower than that of 0.5 kJ/mm weld sample), small PAGES, and low solute level in the retransformed austenite. Although the accelerated cooling during TMCP is not very high, the pancake shape of the large austenite grains and the higher level of solutes result in a lower overall transformation temperature and, therefore, a higher hardness than that of the

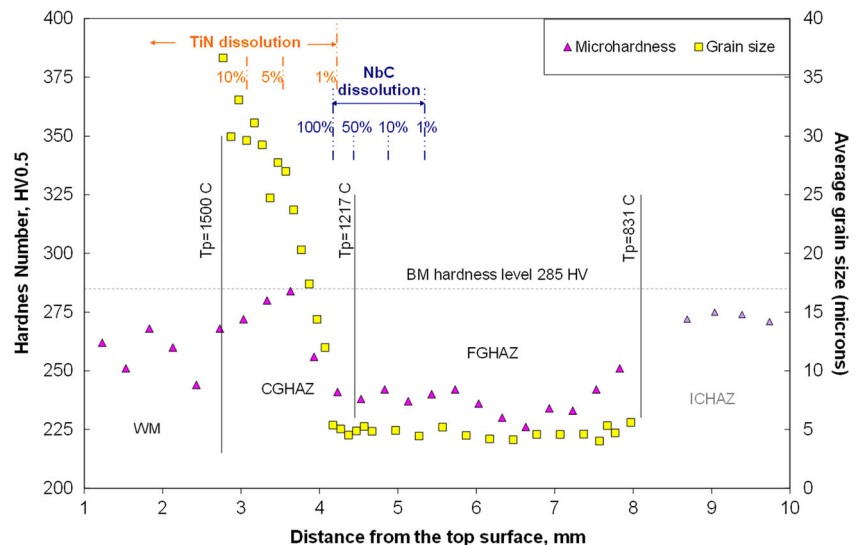
inner FGHAZ. Further dissolution of V, Mo, and Fe carbides in the outer FGHAZ will increase the amount of solutes and hardenability beyond a critical point (for the cooling rate and PAGES in this sample) and result in a higher hardness level at the outer FGHAZ.

At higher heat inputs (1.0 kJ/mm and above), the transformation in FGHAZ is likely insensitive to the C level (in the range where it changed) due to the relatively low cooling rates. There was a hardness plateau in the FGHAZ for these samples (Figs. 2 and 12). The microstructure was made up of polygonal ferrite with an average grain size of ~ 1.5 μm across the entire FGHAZ for the 1.5 and 2.5 kJ/mm weld samples (~ 800 $^{\circ}\text{C} < T_p < 1240$ $^{\circ}\text{C}$).

4.2.3 CGHAZ

All the hardness traverses (Fig. 2) showed hardening in the CGHAZ relative to the FGHAZ. They showed a sudden

Fig. 12 HAZ property diagram for a heat input of 2.5 kJ/mm; see the caption of Fig. 11 for the explanation of the precipitate dissolution marks



increase starting from the boundary between the FGHAZ and CGHAZ and reached a peak somewhere in the CGHAZ and then decreased slightly towards the fusion line. The onset of the increase in hardness virtually coincided with the onset of an increase in grain size for all samples (Figs. 11 and 12). These alterations can be better tracked and explained for the 0.5 kJ/mm weld sample, where longitudinal mapping provided a detailed account of hardness variation across the CGHAZ (Fig. 3). The hardenability increases with PAGS, resulting in a higher average microhardness. Microhardness reached a maximum of ~ 360 HV0.5 at a PAGS of ~ 13 μm and T_p of ~ 1170 $^{\circ}\text{C}$. At this point, all Mo, V, and Fe carbides should be dissolved (NbC dissolution starts just above this temperature, as marked in Fig. 11). This makes the matrix sufficiently rich in C (0.064%, as estimated from theoretical calculation [14]) to promote the formation of martensite for such a cooling rate (100–200 $^{\circ}\text{C}/\text{s}$). As the peak temperature increases beyond this point, the microhardness starts to decline gradually and steadily towards the fusion line, where it reaches an average microhardness of ~ 340 HV0.5. This occurs while the PAGS keeps rising towards the fusion line where it reaches a maximum of ~ 32 μm on average. The carbon level in austenite increases to a maximum level of 0.08% at $T_p = 1320$ $^{\circ}\text{C}$ and remains constant afterwards. The increase in PAGS beyond a critical value (~ 13 μm here) results in a decrease in hardness, likely due to the hardness dependence of martensite on morphological parameters such as lath block size, packet size, and PAGS. In the context of the Hall-Petch equation, strength and hardness decrease as the grain size increases.

The same general scenario should apply to the CGHAZ of the other weld samples with different lath-like microstructures such as bainite. The maximum hardness, however, decreases as the heat input increases (Fig. 4), due to the increase in transformation temperature as a result of a decrease in cooling rate. Replacement of lath martensite with lower bainite, upper bainite, and acicular ferrite is accompanied with a drop in hardness and strength as (a) the carbon saturation decreases, (b) the dislocation density decreases, and (c) the effective grain size (lath, block or packet) increases. Nevertheless, the lath sizes in the bainitic ferrite of the 1.5 and 2.5 kJ/mm CGHAZ are small enough (~ 1 – 2 μm in width and several microns in length) to provide hardness levels almost comparable to the BM, even though the packet sizes and the PAGS in this region are very large (several tens of microns reaching a maximum mean intercept length of ~ 37 μm close to the fusion line for the 2.5 kJ/mm weld sample).

The nanohardness contours for the CGHAZ-0.5 kJ/mm sample (Fig. 7) can now be understood better. Microstructural examination of this sub-zone showed two main constituents: (a) fine untempered lath martensite and (b) coarse autotempered martensite or aged massive ferrite. The width and hardness of the band of hard region in Fig. 5 correlate well with the former constituent, while the relatively

soft regions correlate well with the latter constituent (either coarse martensite or massive ferrite). This is due to the low hardenability and high M_s temperature of grade 100 microalloyed steel.

4.3 Grain coarsening temperature and CGHAZ relative width

A parameter of interest in the HAZ is the grain-coarsening temperature (T_{GC}). Different criteria have been proposed in the literature to define this temperature. Among these are the temperature corresponding to an ASTM grain size number of 5 in the CGHAZ and the first appearance of a large area of Widmanstätten ferrite across the HAZ [17]. Since the HAZ of the grade 100 steel exhibited a distinct boundary between the FGHAZ and the CGHAZ, the peak temperature corresponding to this boundary (as determined by interpolation of the experimental thermal analysis results or from the theoretical calculations) would make a practical criterion for T_{GC} . Another parameter that is related to T_{GC} is the relative width of the CGHAZ that can be directly and readily determined from the etched macro-sections.

Although the final PAGS decreased with decreasing heat input, examination of the HAZ revealed that the CGHAZ width fraction increased (from approximately 0.23 to 0.32; Table 4) and T_{GC} decreased (from approximately 1217 to 1134 $^{\circ}\text{C}$, as marked in Figs. 11 and 12) with a decrease in heat input from 2.5 to 0.5 kJ/mm. HAZ grain coarsening consists of two phenomena: reaustenitization and austenite grain growth. With increasing heating rate (as the heat input decreases), superheating above the equilibrium austenite transformation temperature increases. This increases the driving force for austenitization and results in a larger number of austenite grains (i.e., smaller average austenite grain size upon the completion of transformation). Grain growth is a function of the dwell time, which decreases with decreasing heat input, as well as the performance of grain-growth inhibitors. The main three factors that can hinder grain growth in the HAZ are as follows [15]: precipitates, impurity drag, and a temperature gradient (or “thermal pinning”). Precipitates have a grain-boundary pinning effect, until they are coarsened greatly or dissolved. On the other hand, segregation of certain solutes, especially Nb, P, and S, to the grain boundaries exerts additional dragging forces and reduces the mobility of the grain boundaries. This effect can continue after the precipitates are dissolved. Peak temperature gradients exert another hindering force due to the gradient in the grain size profile. It has been suggested that the smaller grains at locations farther from the fusion line exert a pinning force on the larger neighboring grains closer to the fusion line [15]. This is referred to as thermal pinning in some of the literature [18]. With decreasing heat input, the precipitate pinning effect increases (as a result of less precipitate coarsening and dissolution), the solute drag

effect decreases (due to less precipitate dissolution), and the thermal pinning increases (due to the formation of a narrower HAZ).

The decrease in T_{GC} (from approximately 1240 to 1190 °C) with increasing heating rate (from approximately 0.1 to 4 °C/s) was also noted upon heat treatment of a V-Ti microalloyed steel by Siwecki et al. (as cited in [19]). A holding time of 30 min was used in those experiments. Note, however, that the heating rates experienced during welding with heat input values of 0.5–2.5 kJ/mm are orders of magnitude higher (Table 3). In the case of a low heat input (e.g., 0.5 kJ/mm), diffusional nucleation and growth may not happen. It was suggested by Rasanen and Tenkula [20] that rapid heating (200–300 °C/s or more) may lead to a “reverse martensitic transformation” of ferrite to austenite in some cases, and the resulting transformation induced deformation may accelerate grain growth. In this case, the precipitates do not have any major effect on the growth rate.

4.4 Maximum hardness of martensitic structures

The CGHAZ essentially showed a linearly inverse dependence of maximum microhardness on heat input (Fig. 4). This was attributed to the formation of very hard constituents in the microstructure as a result of an increase in cooling rate. Zhu et al. also reported a similar relationship between simulated CGHAZ macrohardness and heat input for a range of heat inputs between 0.8 and 1.7 kJ/mm in an X80 microalloyed steel [21]. The maximum microhardness along the traverses (load of 0.5 kg) was significantly higher for a heat input of 0.3 kJ/mm than for a heat input of 0.4 or 0.5 kJ/mm. The higher CGHAZ hardness for the heat input of 0.3 kJ/mm was likely attributable to a smaller “grain” size (lath block and packet size and PAGS), as well as conceivably a higher fraction of lath martensite (with high dislocation density) and a lower fraction of autotempered martensite or massive ferrite associated with the faster thermal cycle.

A macrohardness number of 355 ± 3 HV5 was obtained for the CGHAZ of the 0.5 kJ/mm sample (Table 5). Additional testing revealed a macrohardness number of approximately 360 HV5 for the CGHAZ of the 0.3 kJ/mm sample. Although the classic graphs like the one shown in Fig. 13 may imply that the hardness of martensite depends only on the carbon content and a hardness value of ~350 HV is associated with a “fully martensitic” structure for a steel with the carbon content of 0.08% [22], this investigation and some other investigations (as discussed below) show that such assumptions or implications may not be valid.

It has been suggested by Galindo-Nava and Rivera-Diaz-del-Castino [10] that the main strengthening contributors in a lath martensitic structure include high-angle grain boundaries (of lath blocks and packets), dislocations (the density of which can be related to carbon content due to carbon segregation),

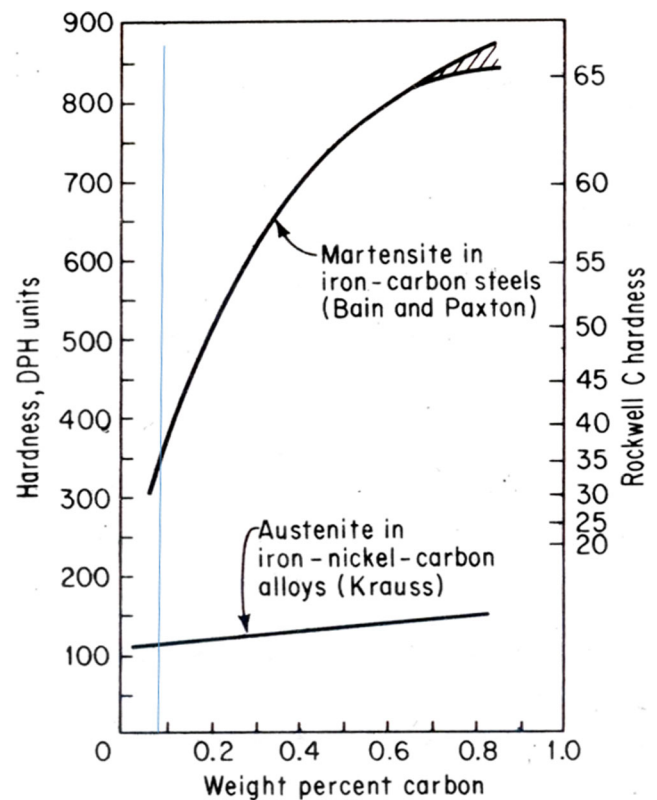


Fig. 13 Variation of martensite hardness with carbon content [22]

and carbide precipitates after tempering (which could include autotempering). They found that solute solution strengthening has a smaller contribution, and it mainly includes the contribution from the substitutional atoms, since interstitials are trapped at lath boundaries (Cottrell atmospheres). The effective grain size for strength is that of a block (i.e., a substructure of a packet that contains several laths), which is proportional to PAGS (block size or $d_{\text{Block}} = 0.067$ PAGS) for a range of PAGS between 10 and 75 μm .

Therefore, a smaller PAGS in a lath martensitic structure (associated with a lower heat input) translates to a smaller block size and packet size ($d_{\text{Packet}} = 0.40$ PAGS) and a higher strength or hardness in the context of the Hall-Petch relationship. This is consistent with our finding that the maximum microhardness in the 0.5 kJ/mm weld sample is observed in the CGHAZ closer to the FGHAZ boundary (than the fusion line). As long as the combination of cooling rate and hardenability is sufficient to produce martensite upon cooling in the HAZ, a smaller PAGS can result in a higher hardness. In fact, it has been shown that in low carbon martensitic steels, the maximum hardness is in the FGHAZ (referred to as “the displaced hardness peak”), since the hardenability is high enough to produce lath martensite in both the CGHAZ and FGHAZ, while the FGHAZ has a smaller effective grain size [23]. This finding questions the validity or thoroughness of most laboratory practices that perform hardness testing adjacent to the fusion line to evaluate the maximum HAZ

hardness, while the maximum hardness may be somewhere between the fusion line and the CGHAZ/FGHAZ boundary. The practice follows the recommendation of some standard specifications (such as NACE MR0175 [24]) that state the hardness indentation in the HAZ should be placed as close as possible to the fusion line.

5 Conclusions

The following main conclusions can be drawn from this investigation, where microstructural examination and macro/micro/nanohardness testing are combined with the results of earlier studies, to generate HAZ property diagrams for a grade 100 microalloyed steel:

- 1) Depending on the heat input, the FGHAZ exhibited hardening (0.5 kJ/mm weld sample), softening (1.0–2.5 kJ/mm weld samples), or a combination of both (0.7 kJ/mm weld sample), with respect to the base metal.
- 2) As expected, the CGHAZ exhibited higher hardness than the FGHAZ regardless of heat input. The higher hardenability in this sub-region was a result of the large PAGS and carbide dissolution, both due to higher peak temperatures.
- 3) There was a gradual decrease in hardness in the CGHAZ towards the fusion line beyond a hardness peak point. This finding puts into question the validity or thoroughness of many laboratory practices that perform hardness testing as close as possible to the fusion line to evaluate HAZ maximum hardness.
- 4) Both the nanohardness contours and microstructural observations suggest that the microstructure in the CGHAZ-0.5 kJ/mm was not 100% martensite. The CGHAZ-0.5 kJ/mm showed two structures, namely fine untempered lath martensite and either coarse autotempered martensite or aged massive ferrite. The untempered lath martensite had a fine structure (200–500 nm in thickness) and was devoid of precipitates. The autotempered martensite or massive ferrite had a coarse structure (2–4 μm in thickness) with cementite particles.
- 5) The relative width of the CGHAZ increased and the grain coarsening temperature decreased with decreasing heat input, although the amount of grain growth (in terms of PAGS) decreased with decreasing heat input.
- 6) The maximum microhardness in the CGHAZ had a linearly inverse relationship with heat input. The maximum hardness in the martensitic structure associated with low heat input samples can exceed the number predicted from classic hardness-carbon concentration graphs.

Acknowledgements The authors wish to thank the Natural Sciences and Engineering Research Council (NSERC) of Canada and Evraz Inc. NA for financial support and steel plates (Evraz).

References

1. Gladman T (1997) The physical metallurgy of microalloyed steels. The Institute of Materials, London
2. Poorhaydari K, Ivey DG (2009) Microstructural examination of a grade 100 microalloyed steel and correlation with yield strength. *Can Metall Q* 48(4):443–454. <https://doi.org/10.1179/cm.2009.48.4.443>
3. Shiga C (1990) Effects of steelmaking, alloying and rolling variables on the HAZ structure and properties in microalloyed plate and Linepipe, presented at the metallurgy, welding, and qualification of microalloyed (HSLA) steel weldments, Houston, Texas
4. Poorhaydari K, Patchett BM, Ivey DG (2005) Estimation of cooling rate in the welding of plates with intermediate thickness. *Weld J* 84: 149-s–155-s
5. Ruhle M (1995) Transmission electron microscopy. In: ASM Handbook. Metallography and microstructures, vol 9. ASM International, Materials Park, pp 103–122
6. Kuhn L (1998) The TriboScope nanomechanical testing system. In: Hysitron nanomechanical test instrument, user's manual, vol NRL-S-003 v1.0. Hysitron Inc, Edina, pp 1–11
7. Hess WF, Merrill LL, Nippes EF Jr, Bunk AP (1943) The measurement of cooling rates associated with arc welding and their application to the selection of optimum welding conditions. *Weld J* 22: 377-s–422-s
8. Poorhaydari K, Ivey DG, Patchett BM (2006) Transformation twins in the weld HAZ of a low-carbon microalloyed steel. *Mater Sci Eng A* 435–436:371–382. <https://doi.org/10.1016/j.msea.2006.07.055>
9. Poorhaydari K, Patchett BM, Ivey DG (2004) Correlation between microstructure and hardness of the weld HAZ in grade 100 microalloyed steel, presented at the 5th international pipeline conference, Calgary, AB
10. Galindo-Nava EI, Rivera-Diaz-del-Castillo PEJ (2015) A model for the microstructure behaviour and strength evolution in lath martensite. *Acta Mater* 98:81–93. <https://doi.org/10.1016/j.actamat.2015.07.018>
11. Deb P, Challenger KD, Clark DR (1986) Transmission electron microscopy characterizations of preheated and non-preheated shielded metal arc weldments of HY-80 steel. *Mater Sci Eng* 77: 155–167. [https://doi.org/10.1016/0025-5416\(86\)90364-2](https://doi.org/10.1016/0025-5416(86)90364-2)
12. Moon DW, Fonda RW, Spanos G (2000) Microhardness variations in HSLA-100 welds fabricated with new ultra-low-carbon weld consumables. *Weld J* 79:278-s–285-s
13. Speich GR, Warlimont H (1968) Yield strength and transformation substructure of low-carbon martensite. *J Iron Steel Inst* 206:385–392
14. Poorhaydari K, Ivey DG (2011) Precipitate alterations in the heat-affected zone of a grade 100 microalloyed steel. *J Mater Sci* 46(14): 4953–4963. <https://doi.org/10.1007/s10853-011-5412-0>
15. Easterling KE (1992) Introduction to the physical metallurgy of welding, 2nd edn. Butterworth-Heinemann Ltd, Oxford
16. Shome M, Gupta OP, Mohanty ON (2004) Effect of simulated thermal cycles on the microstructure of the heat-affected zone in HSLA-80 and HSLA-100 steel plates. *Metall Mater Trans A* 35A: 985–996
17. George ET, Irani JJ (1968) Control of austenitic grain size by additions of titanium. *J Aust Inst Met* 13:94–106

18. Alberry PJ, Chew B, Jnones WKC (1977) Prior austenite grain growth in heat-affected zone of a 0.5Cr-MO-V steel. *Met Technol* 4(1):317–325. <https://doi.org/10.1179/030716977803292619>
19. Lagneborg R, Siwecki T, Zajac S, Hutchinson B (1999) The role of vanadium in microalloyed steels. *Scand J Metall* 28:186–241
20. Rasanen E, Tenkula J (1972) Phase changes in the (arc) welded joints of (low carbon) constructional steels. *Scand J Metall* 1:75–80
21. Zhu Z, Han J, Li H (2015) Influence of heat input on microstructure and toughness properties in simulated CGHAZ of X80 steel manufactured using high-temperature processing. *Metall Mater Trans A* 46A:5467–5475
22. Krause GE (1990) *Properties and selection: irons, steels and high performance alloys*, 10th edn. ASM International, Metals Park
23. Dunne DP, Pang W (2013) Structural and hardness gradients in the heat affected zone of welded low carbon martensitic steels. *Mater Sci Forum* 738-739:206–211. <https://doi.org/10.4028/www.scientific.net/MSF.738-739.206>
24. (2009) *Petroleum and natural gas industries—materials for use in H₂S-containing environments in oil and gas production—part 2—ANSI/NACE MR0175/ISO 15156–2:2009(E)*. pp 18